Titania Tube-in-Tube Scaffolds with Multilength-Scale Structural Hierarchy and Structure-Enhanced Functional Performance

1 AUTHOR:

Yan Xu

Jilin University

24 PUBLICATIONS   **288** CITATIONS

Titania Tube-in-Tube Scaffolds with Multilength-Scale Structural Hierarchy and Structure-Enhanced Functional Performance

Haibo Huang,[†] Yun Wang,[†] Chen Zou,[†] Jiawei Tao,[†] Dan Qu,[†] Xiaoting Ma,[†] Ping Liu,[§] Yizao Wan,[§] and Yan Xu*,[†]

[†]State Key Lab of Inorganic Synthesis and Preparative Chemistry, Jilin University, Changchun 130012, China
[§]Department of Materials Science and Engineering, Tianjin University, Tianjin 300072, China

Ⓢ Supporting Information

ABSTRACT: Hierarchical structuration has proven to be effective in optimizing the functional performance of nanomaterials. Herein, we report for the first time the evolution of a titania tube-in-tube scaffolding architecture with multilength-scale structural hierarchy (TITS TiO$_2$) and structure-enhanced functional performance. The nanoengineering was accomplished by a precursor scaffolding-concurrent epitaxial growth approach using bacterial cellulose (BC) as a bioscaffold. The BC@SiO$_2$@TiO$_2$ precursor scaffold with a sandwiching SiO$_2$ layer plays an essential role in the formation of the tube-in-tube geometry. TITS TiO$_2$ exhibits significantly superior photocatalytic activity to Degussa P25. It shows great UV light absorption ability and high specific surface area, which we believe are responsible for its superior photocatalytic activity. The monolithic nature of TITS TiO$_2$ makes photocatalyst separation and recovery possible. We show that TiO$_2$ nanocrystals can be used as a building block for the organization of complex inorganic nanomaterials with multilength-scale structural hierarchy using a bioscaffold with desired structural features: monolith (millimeter and above), macropore (micrometer), and nanotube/nanopore (nanometer), offering a versatile route for the design of advanced hierarchical nanomaterials.
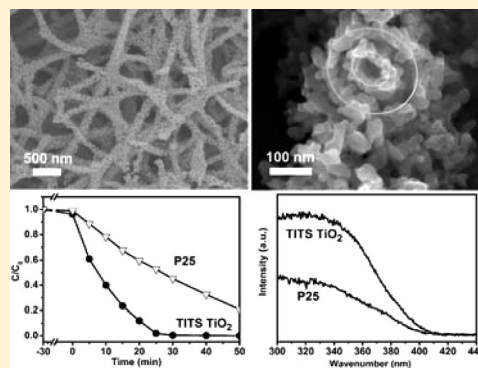
1. INTRODUCTION

Titania (TiO$_2$) has emerged as one of the most promising semiconductor oxides, led by the pioneering discovery of the photocatalytic water splitting phenomenon on TiO$_2$ electrode by Fujishima and Honda in 1972.[1] Owing to its superior photoreactivity, chemical stability, nontoxicity, and low cost, TiO$_2$ materials hold exciting implications for developing sustainable solutions for environmental and energy problems such as detoxification of organic pollutants, solar energy conversion, and renewable energy production.[2−7] Under the irradiation of UV light, TiO$_2$ generates electrons and holes that subsequently turn adsorbed water and oxygen to highly reactive oxygen species causing adhered organic pollutants to decompose. The process takes place under ambient conditions, and no regeneration of photocatalysts is required, rendering TiO$_2$ an ideal environmental catalyst. Although TiO$_2$ possesses such promising potentials, its large-scale adoption for energy and environmental applications has been hampered by low solar light harvesting efficiency due to a wide band gap (3.0−3.2 eV) and relatively poor charge transport property.[8−10]

In general, the photocatalytic activity of semiconductors is controlled by light harvesting, charge separation and transport, surface reaction site, and redox reaction rate. Architecturation of nanomaterials has proven to be effective in modulating materials' properties, such as light interaction, surface reactivity, and charge transport, to deliver optimized functional performance.[11,12] Nanotubular TiO$_2$ materials with varying degrees of structural hierarchy show attractive structure-enhanced performance due to their unique properties, such as good charge transport and large specific surface area, that qualify them for wide-ranging applications from energy harvesting and storage to catalyst design.[13−22] Among others, anodic oxidation,[23,24] electrospinning,[25−27] and hard templating[28−30] are common approaches used for producing TiO$_2$ nanotubes of varying aspect ratios,[31] where nanoengineering of structural hierarchy can be achieved using the Ostwald ripening effect, the Kirkendall effect, and chemical etching.[32,33] More representative examples include TiO$_2$ nanotubes by a solvothermal method using multiwalled carbon nanotubes as a sacrificial template,[34] the tube-in-tube arrays of mesoporous TiO$_2$ by anodization,[24] mesoporous TiO$_2$ nanotubes by solvothermal alcoholysis of TiOSO$_4$,[35,36] nanotubular TiO$_2$/titanate by electrophoretic deposition,[37] TiO$_2$ microspheres with a tube-in-tube nanostructure by anisotropic etching,[38] and mesoporous TiO$_2$ nanotubes based on the Kirkendall effect and cation exchange.[39] Most of the reported nanotubular materials of TiO$_2$ are either discrete nanotubes with single tubular geometry and hierarchically structured walls or discrete nano- or microspheres

based on nanotubular building blocks.[40] Although such TiO$_2$ nanomaterials exhibit enhanced photocatalytic performance, nanosized TiO$_2$ photocatalysts are hard to separate, resulting in poor recyclability and secondary pollution. One solution around has been the inclusion of magnetic nanoparticles to enable photocatalyst separation; however, further recovery of the magnetic nanoparticles remains an issue to be addressed.

It would be ideal to construct TiO$_2$ monoliths from nanotubular building blocks that exhibit integrated advantages of the nanoscale effects, the hierarchical structure-enhanced activity, and the easy recovery of macroscopic monoliths. Such a TiO$_2$ monolith with integrated benefits has, to the best of our knowledge, not yet been explicitly exploited. Here, we report a TiO$_2$ tube-in-tube scaffold with multilength-scale structural hierarchy by a precursor scaffolding-concurrent epitaxial growth approach. The challenges for constructing such a tube-in-tube scaffolding architecture with engineered hierarchical features arise from the anisotropic geometry. It turns out that these challenges can be overcome by judicious design of precursor scaffolds and alkaline etching. We choose bacterial cellulose (BC) aerogel as a bioscaffold due to its abundant hydroxyl groups and hierarchical structure from self-assembled cellulose nanofibers[41−43] and BC@SiO$_2$@TiO$_2$ as the precursor scaffold. The tube-in-tube scaffold is engineered from the BC@SiO$_2$@TiO$_2$ precursor scaffold by controlled etching of SiO$_2$ and TiO$_2$, followed by removal of BC. To demonstrate the structure-enhanced functionality, the photodegradation performance by the TiO$_2$ with tube-in-tube scaffolding architecture, multi-length-scale structural hierarchy, and anatase−rutile junctions (TITS TiO$_2$) has been examined against other TiO$_2$ photocatalysts with different structural features. Notably, TITS TiO$_2$ exhibits superior photocatalytic activity, as manifested by its degradation rate for methyl orange being four times of that of Degussa P25 (P25). The photocatalytic mechanism has been investigated using radical scavengers, UV−vis, XPS, and PL. The ability to design bioscaffolds with desired hierarchical features and surface functionalities will enable the development of wide-ranging complex inorganic nanomaterials displaying multilength-scale structural hierarchy for advanced applications.

2. EXPERIMENTAL SECTION

Materials. D-Glucose anhydrous was purchased from AMRESCO, yeast extract was from OXOID, and lacto-peptone was from Beijing Aoboxing Biotechonology. Monopotassium phosphate, anhydrous acetic acid, sodium hydroxide, ethanol (>99.7%), *tert*-butanol (99%), cetyltrimethylammonium bromide (98.0% CTAB), ammonia (28.0%), ethylenediaminetetraacetic acid (EDTA), and KBrO$_3$ were purchased from Beijing Chemicals. Tetraethyl orthosilicate (99.9% TEOS) and tetraethyl titanate (33−35% TEOT) were purchased from Aladdin. Methyl orange and isopropanol were purchased from Guangfu Fine Chemicals. All chemicals were used as received. BC aerogel was prepared according to reported procedures.[44]

Preparation of TITS TiO$_2$. In a typical experiment, 0.08 g of BC aerogels was immersed in 30 mL of absolute ethanol containing 1.3 g of CTAB and 5.0 mL of ammonia under stirring at room temperature for 30 min, to which 6.0 mL of TEOS was added dropwise. The reaction proceeded at room temperature for 4 h under gentle agitation. White monolith of BC@SiO$_2$ was recovered by thorough washing using deionized water and ethanol, respectively, and oven dried at 90 °C for 3 min. A 0.1 g amount of BC@SiO$_2$ was impregnated in 10.0 mL of 3.0 M TEOT for 2 h under static conditions to allow

thorough infiltration and then agitated vigorously for 2 h to allow the hydrolysis and polycondensation of TEOT to take place. White monolith of BC@SiO$_2$@TiO$_2$ was recovered by repeated washing using deionized water and ethanol, respectively, and oven dried at 60 °C for 20 min. A 0.05 g amount of BC@SiO$_2$@TiO$_2$ was added to 20.0 mL of 1.0 M NaOH solution (aq) and then autoclaved at 150 °C for 0.5−48 h in a 30.0 mL Teflon-lined stainless-steel autoclave. The hydrothermally treated products were washed thoroughly using 0.1 M HCl acid and deionized water and oven dried at 60 °C for 20 min, followed by calcination at 750 °C for 2 h, designated as TITS TiO$_2$. A hydrothermally treated product prepared via a hydrothermal alkaline etching process at 150 °C for 12 h was washed with acid and calcined at 750 °C for 4 h, designated as TiO$_2$ R1.

Characterization. Transmission electron microscopy (TEM) images, high-resolution transmission electron microscopy (HRTEM) images, and integrated energy-dispersive X-ray spectroscopy (EDS) analysis were recorded on a FEI Tecnai G2S-Twin with a field emission gun operating at 200 kV. Scanning electron microscopy (SEM) images were taken on a JEOL JSM 6700F. Powder X-ray diffraction data (XRD) was acquired on a Rigaku D/Max 2550 X-ray diffractometer with Cu Kα radiation (50 kV, 200 mA, λ = 0.15418 nm). Nitrogen adsorption and desorption isotherms were recorded on a Micromeritics ASAP 2420 M system. All samples were degassed at 200 °C for 12 h before measurements. Mesopore size distributions were calculated using density functional theory (DFT) model. Macropore size distribution was calculated based on mercury intrusion porosimetry measurements using a Micromeritics AutoPore IV 9500 system. Ultraviolet−visible (UV−vis) spectra were recorded on a SHIMADZU UV-1800 spectrometer. UV−vis diffuse reflectance spectroscopy was performed on a HITACHI U-4100 spectrophotometer using Al$_2$O$_3$ as reference. X-ray photoelectron spectroscopy (XPS) was performed on an ESCALAB 250 X-ray photoelectron spectrometer using a monochromatic X-ray source. Photoluminescence (PL) spectra were recorded on a FLUOROMAX-4 (HORIBA Jobin Yvon, France). A 5.0 mg amount of samples was dry pressed into self-supporting wafers and illuminated by a He−Cd laser source (325 nm) at room temperature.

Photodegradation Tests. A photocatalytic test was carried out in a photoreactor (XPA Nanjing Xujiang, China) using a 300 W mercury lamp as the UV light source (λ = 365 nm). Methyl orange was selected as a model compound for investigation. A 10.0 mg amount of photocatalyst and 50.0 mL of aqueous dye solution with an initial concentration (C_0) of 5.0 mg L^{-1} were used. All photocatalysts were cut into small pieces using a razor blade while keeping the original architectures intact. In a typical experiment, small pieces of 10.0 mg of TITS TiO$_2$ were dispersed in 50.0 mL of 5.0 mg L^{-1} methyl orange solution, and the suspension was stored in the dark for 30 min under gentle agitation to establish adsorption−desorption equilibrium between the photocatalyst and methyl orange. The suspension was then exposed to UV light at λ = 365 nm, and the concentration of the residual methyl orange (C) was analyzed at a 5 min interval during the reaction by recording the intensity of the absorption band maximum at λ = 464 nm using a UV−vis spectrometer. TITS TiO$_2$ (milled) was prepared by complete destruction of the scaffolding architecture of TITS TiO$_2$. In a separate experiment, selected scavengers were added to the methyl orange solution before

the addition of photocatalyst based on the following concentration: 500.0 mmol L^{-1} isopropanol, 1.0 mmol L^{-1} EDTA, and 3.0 mmol L^{-1} $KBrO_3$. TiO_2 R1, TITS TiO_2 (milled), and P25 were used as references. The same procedures were applied to all photodegradation tests.

3. RESULTS AND DISSCUSION

The evolution of the tube-in-tube scaffolding architecture with multilength-scale structural hierarchy is illustrated in Scheme 1.

Scheme 1. Schematic Illustration of the Evolution of the Tube-in-Tube Scaffolding Architecture with Multilength-Scale Structural Hierarchy by a Precursor Scaffolding-Concurrent Epitaxial Growth Approach
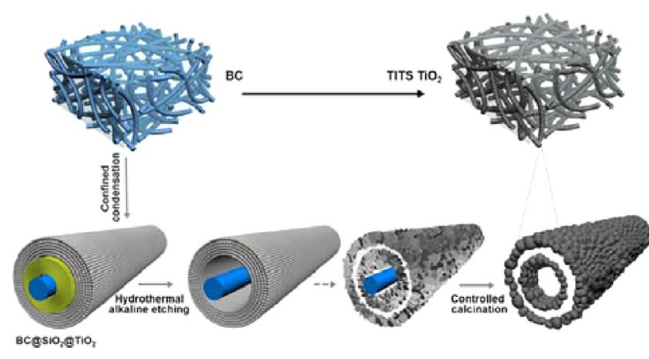
BC with hierarchical structure and surface functionalities mediating and governing mineralization is used as a scaffolding template (see the Supporting Information, Figure S1). BC@SiO_2 was prepared based on the Stöber process using TEOS as a silica source and ammonia as a catalyst (see the Supporting Information, Figures S2a and S2b). It is essential to confine SiO_2 deposition on the surface of BC, for which preloading BC with TEOS and controlled hydrolysis−condensation in ethanol using CTAB as a bridging agent are critical.[45−47] BC@SiO_2 with the SiO_2 layer thickness between 20 and 120 nm has been obtained. Our approach differs from the reported method for making silica-coated filter paper by Huang and co-workers where SiO_2 deposition was done by precoating cellulose with a thin layer of titania.[48] Further deposition of TiO_2 on BC@SiO_2 is achieved by confined hydrolysis−condensation of TEOT, giving rise to the precursor scaffold of BC@SiO_2@TiO_2, where the TiO_2 layer thickness can be tuned between 20 and 100 nm. BC@SiO_2@TiO_2 is constructed from interpenetrating composite fibers of BC@SiO_2@TiO_2 with diameters in the range from 80 to 300 nm (see the Supporting Information, Figure S2c).

The BC@SiO_2@TiO_2 fiber has a sandwich structure as evidenced by the high-magnification TEM imaging analysis (Figure 1a). It consists of a BC core, sandwiching SiO_2 layer, and outer TiO_2 layer with well-defined BC−SiO_2 and SiO_2−TiO_2 interfaces. The deconvoluted XPS peak of O 1s at 531.0 eV is attributed to the Si−O−Ti linkages, confirming the interfacial interaction between the SiO_2 layer and the TiO_2 layer (see the Supporting Information, Figure S3).[49,50] BC@SiO_2@TiO_2 with a diameter of around 200 nm, SiO_2 layer thickness of around 40 nm, and TiO_2 layer thickness of 50 nm is used as a representative for discussion. The BC@SiO_2@TiO_2 precursor scaffold exhibits narrow mesopores centered at 2.5 nm based on the DFT model and broad macropores between 0.1 and 10 μm based on the mercury intrusion porosimetry measurement (see the Supporting Information, Figure S4). The
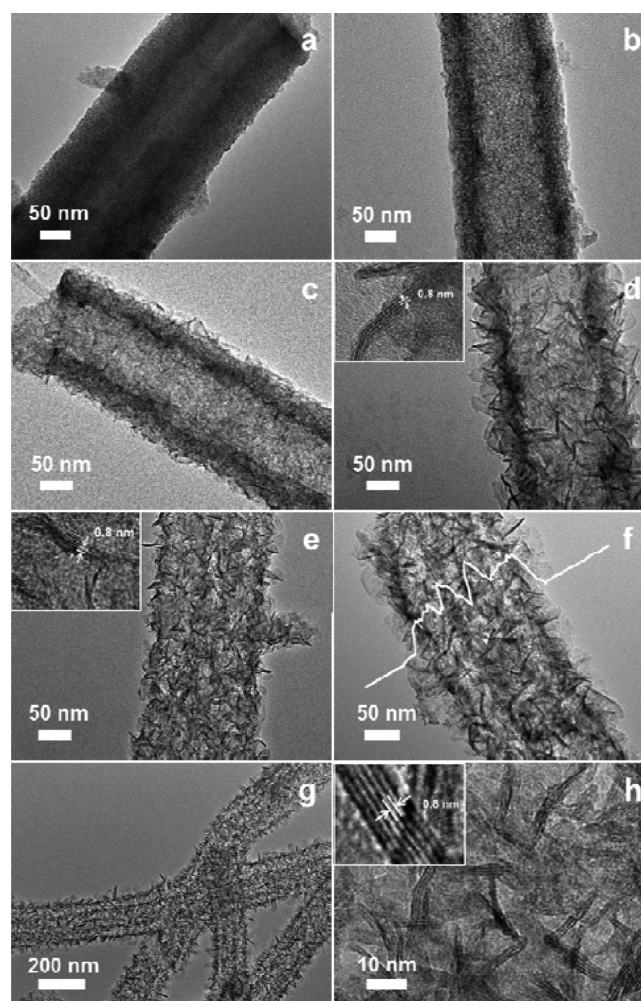
Figure 1. (a) High-magnification TEM image of BC@SiO_2@TiO_2. (b−d) High-magnification TEM images of BC@SiO_2@TiO_2 after hydrothermal alkaline etching at 150 °C for 15 min, 20 min, 6 h, and 12 h, respectively. (d, e, h) Insets: HRTEM showing the lamellar structure. (f−h) Hydrothermal alkaline etching of BC@SiO_2@TiO_2 at 150 °C for 24 h. (f) High-magnification TEM image with cross-sectional EDS line scan of titanium confirming the tube-in-tube geometry. (g) TEM image showing the interpenetration of the tube-in-tube fibers. (h) HRTEM showing the lamellar structure.

mesopores are textural pores formed by packing of SiO_2 and TiO_2 nanoparticles, and the macropores are formed by the interpenetration of the BC@SiO_2@TiO_2 composite fibers. The macropores of BC@SiO_2@TiO_2 are centered at 0.55 μm, which is significantly downshifted compared to those of BC with the macropores centered at 45 μm (see the Supporting Information, Figure S4). It indicates that inorganic condensation involves the hydroxyl hydrogen and oxygen of BC, causing a significant reassembly of cellulose nanofibers and consequential modulation of macropore profile. The BET surface area of BC@SiO_2@TiO_2 is calculated to be 548.3 m^2 g^{-1}, which is significantly greater than that of BC (166.3 m^2 g^{-1}),[44] further confirming that packing of inorganic nanoparticles is responsible for the mesopores and associated large specific surface area.

The BC@SiO_2@TiO_2 precursor scaffold is deliberately designed with a sandwiching SiO_2 layer and outer TiO_2 layer to enable the formation of tube-in-tube geometry. Hydrothermal alkaline etching at 150 °C for 15 min completely

removes the SiO$_2$ layer, leaving the TiO$_2$ layer intact based on the high-magnification TEM and EDS analysis (Figure 1b, Supporting Information, Figure S5a). The characteristic diffraction peak of amorphous silica (broad peak centered at 22°) is absent from the XRD pattern, further confirming complete removal of silica (see the Supporting Information, Figure S5b). As the etching proceeds, the nanoparticle-packed TiO$_2$ layer transforms gradually to nanosheets assembly (Figure 1c−f). Layered trititanate becomes evident after 6 h of hydrothermal alkaline etching as indicated by the XRD analysis (see the Supporting Information, Figure S5b).[51,52] This is further confirmed by the HRTEM investigation showing the lamellar structures with a *d* spacing of around 0.8 nm (Figure 1d, 1e, and 1h, insets).[52] A well-developed tube-in-tube geometry containing BC is obtained after 24 h of the hydrothermal alkaline etching at 150 °C based on the high-magnification TEM and cross-sectional EDS line scan of titanium (Figure 1f−h). Prolonging the hydrothermal alkaline etching to 48 h at 150 °C causes curling of the nanosheets driven by excessive surface energy, and the tube-in-tube geometry is no longer visible (see the Supporting Information, Figure S6).[53−55]

The textural properties of the BC@SiO$_2$@TiO$_2$ precursor scaffold after alkaline etching at 150 °C for 24 h are characterized (see the Supporting Information, Figure S7). The nitrogen adsorption−desorption isotherm exhibits a type IV isotherm with a H3 hysteresis loop. The pore size distribution derived from the adsorption branch using the DFT model indicates the presence of multimodal nanopores centered at 22 nm (see the Supporting Information, Figure S7a). Broad macropores are found in the range of 0.1−60 μm based on the mercury intrusion porosimetry measurement (see the Supporting Information, Figure S7b). The nanosheets assembly and the tube-in-tube geometry are responsible for the multimodal nanopores, and the interpenetration of composite fibers accounts for the macropores. The average wall thickness of the inner and outer tube is 25 and 50 nm, respectively (Figure 1f). The average diameter of the inner tube and the shell thickness between the inner and the outer tube is 80 and 45 nm, respectively. The hydrothermal alkaline etching at 150 °C for 24 h serves to nanopattern the fiber surface, generate the tube-in-tube geometry, and modulate the connectivity between the interpenetrating composite fibers of BC@SiO$_2$@TiO$_2$. It upshifts the center of nanopores and broadens the macropore profile compared to those of the BC@SiO$_2$@TiO$_2$ precursor scaffold (see the Supporting Information, Figures S4 and S7). The BET surface area drops from 548.3 to 332.9 m^2 g^{-1} after 24 h of hydrothermal alkaline etching at 150 °C (see the Supporting Information, Table S1).

It is evident that the hydrothermal alkaline etching is responsible for the formation of the tube-in-tube geometry. Under hydrothermal alkaline conditions, amorphous SiO$_2$ dissolves rapidly and completely, giving rise to a TiO$_2$ ring. The two surfaces of the TiO$_2$ ring in contact with NaOH solution transform to layered trititanate.[51] The trititanate phase grows concurrently on both surfaces of the TiO$_2$ ring. As it proceeds, NaOH solution permeates through the trititanate phase from both sides, causing dissolution of the sandwiched TiO$_2$ nanoparticles. Concurrent epitaxial growth of the trititanate phase on both sides of the TiO$_2$ ring pulls in opposite direction, leading to eventual formation of two trititanate rings. To substantiate the concurrent epitaxial growth hypothesis, a control experiment was carried out using BC@

TiO$_2$ as a precursor scaffold to observe the structural evolution under hydrothermal alkaline conditions at 150 °C for a prolonged period. As shown in Figure S8, Supporting Information, the structure of BC@TiO$_2$ evolves from nanoparticle-packed fibers to nanosheet-assembled fibers, and no tube-in-tube geometry is observed after 24 h. Hydrothermal alkaline etching transforms the external surface of the TiO$_2$ layer to the trititanate phase whose outbound growth is provided by dissolved amorphous TiO$_2$. There is no gap between BC and TiO$_2$; therefore, epitaxial growth of the trititanate phase happens single sidely. This result also confirms that the sandwiching SiO$_2$ layer of the BC@SiO$_2$@TiO$_2$ precursor scaffold plays an essential role in the formation of the tube-in-tube geometry.

The tube-in-tube BC/trititanate is converted to tube-in-tube TiO$_2$ after acid washing and controlled calcination. BC nanofibers are removed; a well-developed scaffolding architecture constructed from interpenetrating tube-in-tube fibers of crystalline TiO$_2$ is obtained, designated as TITS TiO$_2$ (Figure 2a and 2b). Both the inner tube and the outer tube show a
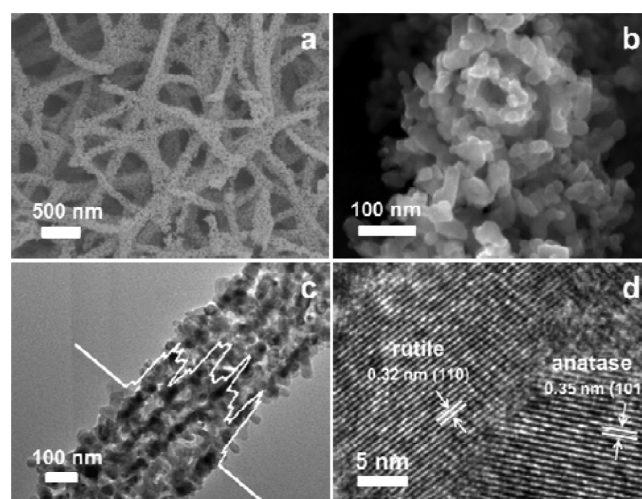

Figure 2. (a) SEM image of TITS TiO$_2$. (b) High-magnification SEM showing tube-in-tube geometry of TITS TiO$_2$. (c) High-magnification TEM image with EDS line scan showing titanium distribution across the tube-in-tube geometry of TITS TiO$_2$. (d) HRTEM showing well-crystallized anatase and rutile and well-defined anatase−rutile interface.

rugged surface with an average diameter of around 70 and 200 nm, respectively. The tube-in-tube geometry is confirmed by the high-magnification TEM and cross-sectional EDS line scan of titanium (Figure 2c). The TiO$_2$ nanocrystals are composed of highly crystalline anatase and rutile at a ratio of 87:13 based on XRD analysis (see the Supporting Information, Figure S9). The average *d* spacing of the lattice fringes of 0.35 and 0.32 nm agrees with the d_{101} planes of TiO$_2$ anatase (JCPDS 21-1272) and the d_{110} planes of TiO$_2$ rutile (JCPDS 87-920), respectively, and the anatase−rutile junction is clearly visible on the HRTEM image taken from the outer tube (Figure 2d). For verification, the inner tube of TITS TiO$_2$ was further examined using HRTEM where the anatase and rutile phases and the anatase−rutile junction are clearly visible (see the Supporting Information, Figure S10).

TITS TiO$_2$ exhibits hierarchical porosity with narrow nanopores centered at 68 nm and broad macropores between 0.1 and 170 μm based on the DFT model and the mercury porosimetry measurement, respectively (Figure 3). The BET
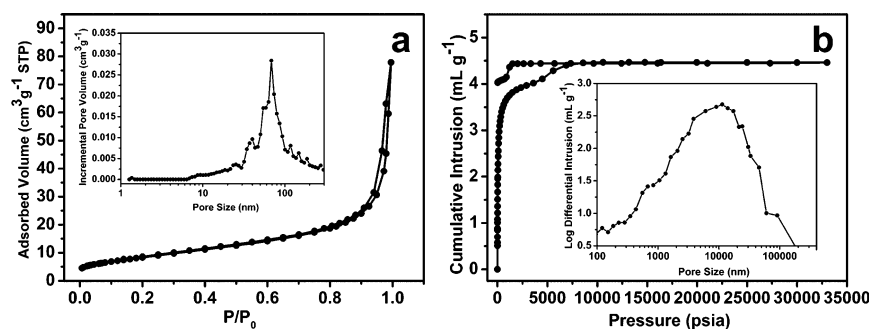
Figure 3. (a) Nitrogen adsorption−desorption isotherm of TITS TiO$_2$. Inset: Nanopore profile. (b) Mercury intrusion porosimetry measurement of TITS TiO$_2$. Inset: Macropore profile.

surface area of TITS TiO$_2$ is calculated to be 75.8 m^{2}g^{-1}. Compared to the alkaline-etched BC@SiO$_2$@TiO$_2$ (332.9 m^{2}g^{-1}), calcination causes a significant reduction in the BET surface area and an upshift of nanopores (Figure 3a, Supporting Information, Figure S7a). The change in the textural properties associated with the nanopores may be ascribable to the nanostructural transformation from nanosheets assembly to intergrown nanocrystals. A slight change in the macropore profile has occurred to TITS TiO$_2$ compared to that of the hydrothermally etched BC@SiO$_2$@TiO$_2$, reflecting that calcination modulates the connectivity between interpenetrating tube-in-tube fibers of TiO$_2$ (Figure 3b, Supporting Information, Figure S7b). We demonstrate that TiO$_2$ nanocrystals can be organized into a tube-in-tube scaffolding architecture by simultaneously replicating multilength-scale structural features, namely, nanotube and nanopore (nanometer), macropore (micrometer), and monolith (millimeter and above), making TITS TiO$_2$ a true nanomaterial monolith with multilength-scale structural hierarchy. The nanopores, nanotubes, and macropores are interconnected.

The unique tube-in-tube scaffolding architecture with multilength-scale structural hierarchy may lead to structure-enhanced functional performance. Calcination of the alkaline-treated and acid-washed BC@SiO$_2$@TiO$_2$ at 750 °C for 2 h gives TITS TiO$_2$ containing anatase/rutile phases at a molar ratio of 87:13. It exhibits the best photodegradation activity and, hence, is used as the photocatalyst for the investigation of the structure-dependent functional performance (see the Supporting Information, Figure S11 and Table S2). TITS TiO$_2$ was tested for the degradation of organic dyes under irradiation of UV light, and the results were compared with those of the references including TiO$_2$ R1, TITS TiO$_2$ (milled), and P25. For ease of comparison, reference photocatalysts were deliberately made to a mixed anatase/rutile phase of similar ratio based on XRD analysis (Figure 4). The BET surface areas of all photocatalysts are summarized in Table S1, Supporting Information.

As shown in Figure 5, TITS TiO$_2$ degrades 100% of methyl orange in 25 min under UV light irradiation (Figure 5a and 5b). TiO$_2$ R1 and P25 degrade about 97% and 80% of methyl orange, respectively, in 50 min under the same test conditions. The reaction kinetics of methyl orange is studied quantitatively by applying the pseudo-first-order model as expressed by the following equation

$$\ln(C_0/C) = kt$$

where k is the pseudo-first-order rate constant. As shown in Figure 5c, the corresponding reaction rate constants, k, are
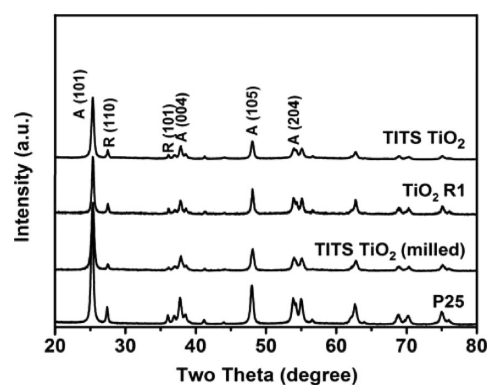

Figure 4. XRD patterns of TITS TiO$_2$, TiO$_2$ R1, TITS TiO$_2$ (milled), and P25.

calculated to be 0.1025, 0.0492, and 0.0257 min^{-1} for TITS TiO$_2$, TiO$_2$ R1, and P25, respectively. The photocatalytic activity of TITS TiO$_2$ remains literally unchanged after 8 recycling runs, indicating good performance stability (Figure 5d). The photocatalytic activity in the destruction of methyl orange under UV light is in a descending order of TITS TiO$_2$ > TiO$_2$ R1 > P25. It is noteworthy that the degradation rate of methyl orange by TITS TiO$_2$ is about four times of that of P25. To establish more convincing evidence of proof for the structure-enhanced photocatalytic activity, the tube-in-tube scaffolding architecture of TITS TiO$_2$ was completely destroyed, designated as TITS TiO$_2$ (milled), with the photocatalytic activity investigated. As shown in Figure 5a, TITS TiO$_2$ (milled) shows drastically reduced photocatalytic activity in the destruction of methyl orange compared to TITS TiO$_2$. The corresponding reaction rate constant is calculated to be 0.0048 min^{-1}, which is about 5% of that of TITS TiO$_2$ (Figure 5c).

To further understanding of the structure-enhanced photocatalytic performance, the optical property of the photocatalysts was investigated using UV−vis spectroscopy. As shown in Figure 6a, the light absorption intensity is in a descending order of TITS TiO$_2$ > TiO$_2$ R1 > P25 > TITS TiO$_2$ (milled). TITS TiO$_2$ has a tube-in-tube scaffolding architecture with an inner tube diameter and shell thickness of 85 and 40 nm, respectively (Figure 2b). TiO$_2$ R1 has a single-tube scaffolding architecture (Figure 6b, Supporting Information, Figure S12). TITS TiO$_2$ (milled) and P25 contain nanocrystals with an average size of 22 and 23 nm, respectively, from the high-magnification TEM (Figure 6c and 6d). We believe that the tube-in-tube scaffolding architecture of TITS TiO$_2$ causes multiple light reflection and scattering that are responsible for its strong light absorption
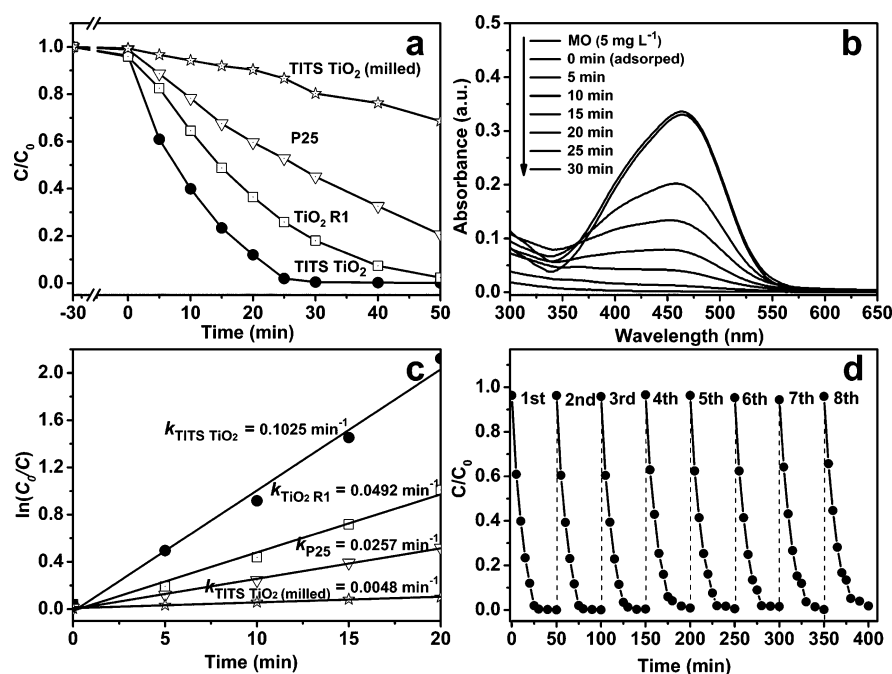
Figure 5. (a) Photocatalytic degradation of methyl orange as a function of irradiation time under UV light in the presence of TITS TiO$_2$, TiO$_2$ R1, TITS TiO$_2$ (milled), and P25. (b) Absorption spectrum of methyl orange as a function of irradiation time in the presence of TITS TiO$_2$. (c) The corresponding reaction rate constants k. (d) Cycling runs of TITS TiO$_2$ in the photocatalytic degradation of methyl orange.
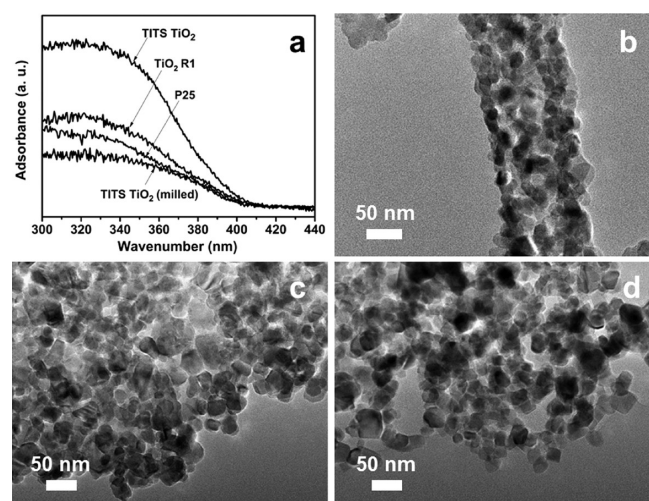

Figure 6. (a) UV−vis diffuse reflectance spectra of the photocatalysts. High-magnification TEM images: (b) TiO$_2$ R1 showing the single-tube geometry, (c) TITS TiO$_2$ (milled), and (d) P25 showing the nanocrystals.

activity. All photocatalysts are well crystallized. Our results manifest that hierarchical structuration affords to modulate light harvesting ability that contributes to enhance the photocatalytic activity of the TiO$_2$ photocatalysts.

To gain more insight of the photocatalytic mechanism, the effect of radical scavengers on the photodegradation of methyl orange was investigated. Isopropanol is a well-known scavenger for hydroxyl radical ($^{\bullet}$OH), EDTA for photogenerated holes (h$^+$), and KBrO$_3$ for superoxide radical ($^{\bullet}$O$_2^-$).[56] As shown in Figure 7, the addition of isopropanol causes the most significant
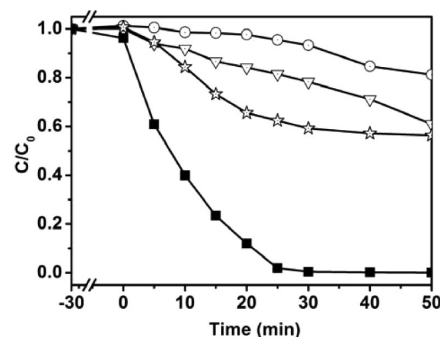

Figure 7. Effect of scavengers on the photodegradation of methyl orange using TITS TiO$_2$ as a photocatalyst: (■) without scavenger, (○) isopropanol as a scavenger, (▽) EDTA as a scavenger, and (☆) KBrO$_3$ as a scavenger.

ability. This assumption is supported by the fact that TITS TiO$_2$ with the tube-in-tube geometry is a better light absorber than TiO$_2$ R1 with the single-tube geometry as evidenced by the UV light absorption intensity (Figure 6a). The BET surface area of the photocatalysts is in a descending order of TITS TiO$_2$ (75.8 m^2 g^{-1}) > TITS TiO$_2$ (milled) (64.7 m^2 g^{-1}) > TiO$_2$ R1 (58.9 m^2 g^{-1}) > P25 (47.8 m^2 g^{-1}), which makes TITS TiO$_2$ a favorable choice as a photocatalyst due to the fact that the photocatalytic process is a surface reaction. The fact that TiO$_2$ R1 with single-tube geometry shows superior photocatalytic activity to TITS TiO$_2$ (milled) containing nanocrystals despite its lower specific surface area provides additional evidence of support for the structure-enhanced photocatalytic

loss of degradation activity, indicating that $^{\bullet}$OH is the most active species. The addition of EDTA, which is an effective blocker for h$^+$, results in an evident loss of reactivity, suggesting that h$^+$ plays a critical role in the photodegradation of methyl orange. Being a strong oxidant, KBrO$_3$ is an effective electron acceptor that competes with oxygen. Addition of KBrO$_3$ leads to a loss of degradation efficiency by 36% in 25 min, implying that $^{\bullet}$O$_2^-$ is a very active species.
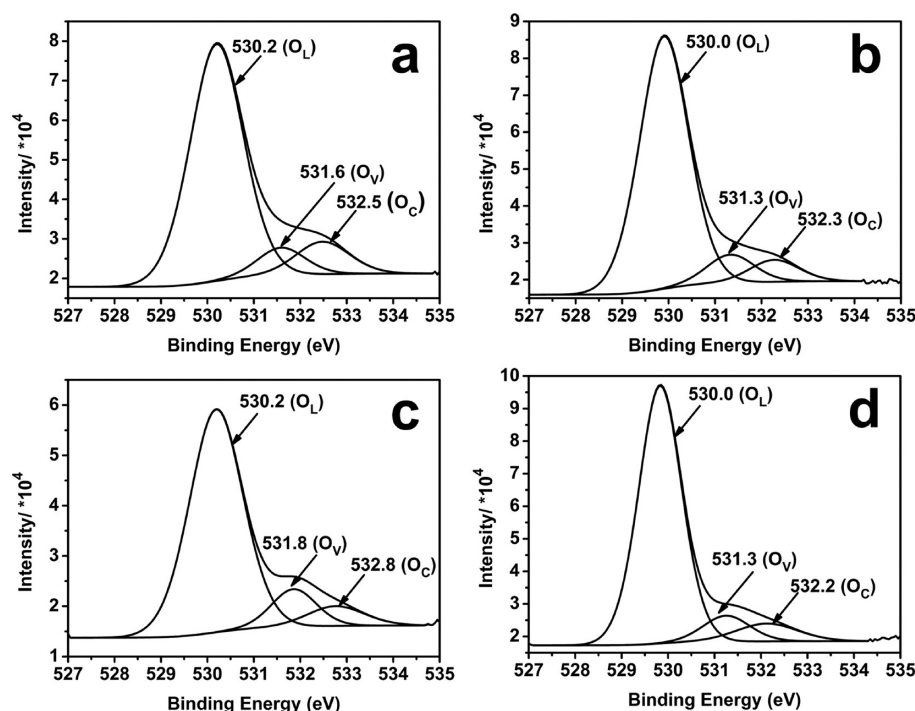
Figure 8. XPS analysis, the deconvoluted XPS peaks of O 1s: (a) TITS TiO$_2$, (b) TiO$_2$ R1, (c) TITS TiO$_2$ (milled), and (d) P25.

The surface and subsurface components and oxidation states of the TiO$_2$ photocatalysts were investigated using XPS. As shown in Figure 8, the XPS peaks of O 1s of all the photocatalysts are asymmetrical, and they can be deconvoluted into three component peaks by fitting to a Gaussian function with the binding energy centered around 530, 531, and 532 eV. These O 1s peaks are assigned to lattice oxygen (O$_L$, 530 eV), oxygen vacancies or defects (O$_V$, 531 eV), and chemisorbed or dissociated oxygen species (O$_C$, 532 eV).[57,58] It is known that the surface oxygen vacancies or defects and chemisorbed oxygen species trap photogenerated charge carriers, serving to enhance the photocatalytic activity of photocatalysts.[59] Our results show that surface oxygen vacancies or defects and chemisorbed oxygen species exist in all the TiO$_2$ photocatalysts, which contribute to their photocatalytic activity.

To verify the XPS results, PL emission spectroscopy was used to investigate the charge separation and surface defects of the TiO$_2$ photocatalysts. In general, the PL emissions of semiconductors are originated from band−band PL emission and excitonic PL emission.[60,61] The band−band PL emission reflects the separation of photogenerated electrons and holes. The excitonic PL emission results mainly from surface oxygen vacancies and defects that bind photogenerated electrons to form excitons in the sub-bands. For TiO$_2$ anatase and rutile, the band−band PL emission is typically around 400 nm and the excitonic PL emission is in visible light region. As shown in Figure 9, the excitonic PL emission bands of the photocatalysts are broad in the visible light region with the emission intensity in an ascending order of TITS TiO$_2$ < TiO$_2$ R1 < P25 < TITS TiO$_2$ (milled), indicating a decrease in the amount of surface oxygen vacancy or defect. The PL results suggest that surface defects exist in all photocatalysts, and TITS TiO$_2$ has the least amount of surface defects compared to the rest of the TiO$_2$ photocatalysts.

It is evident that the tube-in-tube geometry of TITS TiO$_2$ is a favorable attribute for photocatalytic applications. The
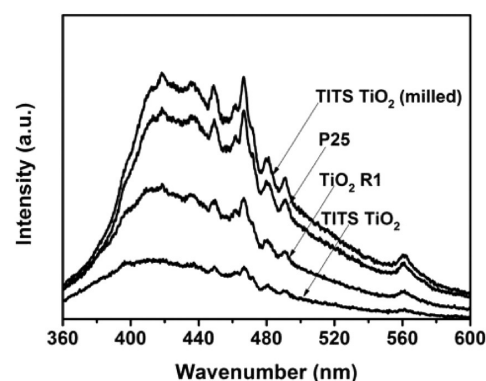

Figure 9. PL emission spectrum of TITS TiO$_2$, TiO$_2$ R1, TITS TiO$_2$ (milled), and P25.

structure-enhanced photocatalytic performance has been evidenced by the superior photocatalytic activity of TITS TiO$_2$ to TiO$_2$ R1 with a single-tube scaffolding architecture and P25-containing nanocrystals. The hydroxyl radicals, photo-generated holes, and superoxide radicals in TITS TiO$_2$ generated under irradiation of UV light serve as active species degrading organic dyes. TITS TiO$_2$ exhibits high UV-light absorption ability and high specific surface areas, which we believe are mainly responsible for its excellent photocatalytic activity and performance stability. As an added advantage, the monolithic nature of TITS TiO$_2$ makes photocatalyst separation and recycling possible, highlighting the unique contributions of the current work.

4. CONCLUSION

In summary, the evolution of a titania tube-in-tube scaffolding architecture with multilength-scale structural hierarchy has been investigated. It is achieved by a precursor scaffolding-concurrent epitaxial growth approach using bacterial cellulose as a bioscaffold. The BC@SiO$_2$@TiO$_2$ precursor scaffold with a

sandwiching SiO_2 layer plays an essential role in the nanoengineering of the tube-in-tube scaffolding architecture under hydrothermal alkaline conditions. The titania tube-in-tube scaffolds with multilength-scale structural hierarchy exhibit strong UV light absorption, high specific surface area and monolith that account for its superior photocatalytic activity, excellent performance stability, and ease of photocatalyst separation. We demonstrate that multilength-scale structuration affords a powerful means to manipulate the functional performance of nanomaterials. Further investigation is in progress to establish a more insightful view of the quantitative correlation between the geometric parameters of the tubes and the light harvesting capability. We envisage that the bioinspired materials strategy may prove its versatility for developing complex inorganic nanomaterials with multilength-scale structural hierarchy and multifunctionality.

ASSOCIATED CONTENT

Ⓢ Supporting Information

The Supporting Information is available free of charge on the ACS Publications website at DOI: 10.1021/acs.jpcc.5b04125.

AUTHOR INFORMATION

Corresponding Author

*Phone: +86 431 89228929. E-mail: yanxu@jlu.edu.cn.

Author Contributions

The manuscript was written through contributions of all authors. All authors have given approval to the final version of the manuscript.

Notes

The authors declare no competing financial interest.

ACKNOWLEDGMENTS

REFERENCES

(1) Fujishima, A.; Honda, K. Electrochemical Photolysis of Water at a Semiconductor Electrode. *Nature* **1972**, *238*, 37−38.

(2) Khan, S. U. M.; Al-Shahry, M.; Ingler, W. B. Efficient Photochemical Water Splitting by a Chemically Modified n-TiO_2. *Science* **2002**, *297*, 2243−2245.

(3) Armstrong, A. R.; Armstrong, G.; Canales, J.; García, R.; Bruce, P. G. Lithium-Ion Intercalation into TiO_2-B Nanowires. *Adv. Mater.* **2005**, *17*, 862−865.

(4) Xian, J.; Li, D.; Chen, J.; Li, X.; He, M.; Shao, Y.; Yu, L.; Fang, J. TiO_2 Nanotube Array-Graphene-CdS Quantum Dots Composite Film in Z-Scheme with Enhanced Photoactivity and Photostability. *ACS Appl. Mater. Interfaces* **2014**, *6*, 13157−13166.

(5) O'Regan, B.; Gratzel, M. A Low-Cost, High-Efficiency Solar Cell Based on Dye-Sensitized Colloidal TiO_2 Films. *Nature* **1991**, *353*, 737−740.

(6) Chen, J.; Cheng, F. Y. Combination of Lightweight Elements and Nanostructured Materials for Batteries. *Acc. Chem. Res.* **2009**, *42*, 713−723.

(7) Chen, X.; Mao, S. S. Titanium Dioxide Nanomaterials: Synthesis, Properties, Modifications, and Applications. *Chem. Rev.* **2007**, *107*, 2891−2959.

(8) Hagfeldt, A.; Graetzel, M. Environmental Applications of Semiconductor Photocatalysis. *Chem. Rev.* **1995**, *95*, 49−68.

(9) Asahi, R.; Morikawa, T.; Ohwaki, T.; Aoki, K.; Taga, Y. Visible-Light Photocatalysis in Nitrogen-Doped Titanium Oxides. *Science* **2001**, *293*, 269−271.

(10) Chen, X.; Shen, S.; Guo, L.; Mao, S. S. Semiconductor-Based Photocatalytic Hydrogen Generation. *Chem. Rev.* **2010**, *110*, 6503−6570.

(11) Banin, U.; Ben-Shahar, Y.; Vinokurov, K. Hybrid Semiconductor-Metal Nanoparticles: From Architecture to Function. *Chem. Mater.* **2014**, *26*, 97−110.

(12) Yang, H. G.; Zeng, H. C. Synthetic Architectures of TiO_2/$H_2Ti_5O_{11}$·H_2O, ZnO/$H_2Ti_5O_{11}$·H_2O, ZnO/TiO_2/$H_2Ti_5O_{11}$·H_2O, and ZnO/TiO_2 Nanocomposites. *J. Am. Chem. Soc.* **2005**, *127*, 270−278.

(13) Wang, X. D.; Li, Z. D.; Shi, J.; Yu, Y. H. One-Dimensional Titanium Dioxide Nanomaterials: Nanowires, Nanorods, and Nanobelts. *Chem. Rev.* **2014**, *114*, 9346−9384.

(14) Boettcher, S. W.; Spurgeon, J. M.; Putnam, M. C.; Warren, E. L.; Turner-Evans, D. B.; Kelzenberg, M. D.; Maiolo, J. R.; Atwater, H. A.; Lewis, N. S. Energy-Conversion Properties of Vapor-Liquid-Solid-Grown Silicon Wire-Array Photocathodes. *Science* **2010**, *327*, 185−187.

(15) Lee, K.; Mazare, A.; Schmuki, P. One-Dimensional Titanium Dioxide Nanomaterials: Nanotubes. *Chem. Rev.* **2014**, *114*, 9385−9454.

(16) Imai, H.; Takei, Y.; Shimizu, K.; Matsuda, M.; Hirashima, H.; Hirashima, H. Direct Preparation of Anatase TiO_2 Nanotubes in Porous Alumina Membranes. *J. Mater. Chem.* **1999**, *9*, 2971−2972.

(17) Kobayashi, S.; Hamasaki, N.; Suzuki, M.; Kimura, M.; Shirai, H.; Hanabusa, K. Preparation of Helical Transition-Metal Oxide Tubes Using Organogelators as Structure-directing Agents. *J. Am. Chem. Soc.* **2002**, *124*, 6550−6551.

(18) Macák, J. M.; Tsuchiya, H.; Schmuki, P. High-Aspect-Ratio TiO_2 Nanotubes by Anodization of Titanium. *Angew. Chem., Int. Ed.* **2005**, *44*, 2100−2102.

(19) Eder, D.; Kinloch, I. A.; Windle, A. H. Pure Rutile Nanotubes. *Chem. Commun.* **2006**, 1448−1450.

(20) Liu, Z. Y.; Zhang, X. T.; Nishimoto, S.; Murakami, T.; Fujishima, A. Efficient Photocatalytic Degradation of Gaseous Acetaldehyde by Highly Ordered TiO_2 Nanotube Arrays. *Environ. Sci. Technol.* **2008**, *42*, 8547−8551.

(21) Foong, T. R. B.; Shen, Y. D.; Hu, X.; Sellinger, A. Template-Directed Liquid ALD Growth of TiO_2 Nanotube Arrays: Properties and Potential in Photovoltaic Devices. *Adv. Funct. Mater.* **2010**, *20*, 1390−1396.

(22) Tian, G. H.; Chen, Y. J.; Bao, H. L.; Meng, X. Y.; Pan, K.; Zhou, W.; Tian, C. G.; Wang, J. Q.; Fu, H. G. Controlled Synthesis of Thorny Anatase TiO_2 Tubes for Construction of Ag-AgBr/ TiO_2 Composites as Highly Efficient Simulated Solar-Light Photocatalyst. *J. Mater. Chem.* **2012**, *22*, 2081−2088.

(23) Xu, X. J.; Tang, C. C.; Zeng, H. B.; Zhai, T. Y.; Zhang, S. Q.; Zhao, H. J.; Bando, Y.; Golberg, D. Structural Transformation, Photocatalytic, and Field-Emission Properties of Ridged TiO_2 Nanotubes. *ACS Appl. Mater. Interfaces* **2011**, *3*, 1352−1358.

(24) Xu, X. J.; Fang, X. S.; Zhai, T. Y.; Zeng, H. B.; Liu, B. D.; Hu, X. Y.; Bando, Y.; Golberg, D. Tube-in-Tube TiO_2 Nanotubes with Porous Walls: Fabrication, Formation Mechanism, and Photocatalytic Properties. *Small* **2011**, *7*, 445−449.

(25) Lu, B. G.; Zhu, C. Q.; Zhang, Z. X.; Lan, W.; Xie, E. Q. Preparation of Highly Porous TiO_2 Nanotubes and Their Catalytic Applications. *J. Mater. Chem.* **2012**, *22*, 1375−1379.

(26) Lang, L. M.; Wu, D.; Xu, Z. Controllable Fabrication of TiO_2 1D-Nano/Micro Structures: Solid, Hollow, and Tube-in-Tube Fibers by Electrospinning and the Photocatalytic Performance. *Chem. - Eur. J.* **2012**, *18*, 10661−10668.

(27) Wu, J.; Wang, N.; Zhao, Y.; Jiang, L. Electrospinning of Multilevel Structured Functional Micro-/Nanofibers and Their applications. *J. Mater. Chem. A* **2013**, *1*, 7290−7305.

(28) Fan, J. J.; Zhao, L.; Yu, J. G.; Liu, G. The Effect of Calcination Temperature on The Microstructure and Photocatalytic Activity of

TiO$_2$-Based Composite Nanotubes Prepared by an in situ Template Dissolution Method. *Nanoscale* **2012**, *4*, 6597−6603.

(29) Berrigan, J. D.; Kang, T. S.; Cai, Y.; Deneault, J. R.; Durstock, M. F.; Sandhage, K. H. Protein-enabled Layer-by-Layer Syntheses of Aligned, Porous-Wall, High-Aspect-Ratio TiO$_2$ Nanotube Arrays. *Adv. Funct. Mater.* **2011**, *21*, 1693−1700.

(30) Xin, L.; Liu, Y.; Li, B. J.; Zhou, X.; Shen, H.; Zhao, W. X.; Liang, C. L. Constructing Hierarchical Submicrotubes From Interconnected TiO$_2$ Nanocrystals for High Reversible Capacity and Long-Life Lithium-Ion batteries. *Sci. Rep.* **2014**, *4*, 4479−4485.

(31) Park, J. H.; Kim, S.; Bard, A. J. Novel Carbon-Doped TiO$_2$ Nanotube Arrays with High Aspect Ratios for Efficient Solar Water Splitting. *Nano Lett.* **2006**, *6*, 24−28.

(32) Fan, H. J.; Gösele, U.; Zacharias, M. Formation of Nanotubes and Hollow Nanoparticles Based on Kirkendall and Diffusion Processes: A Review. *Small* **2007**, *3*, 1660−1671.

(33) Wang, J. W.; Xu, G. Q.; Zhang, X.; Lv, J.; Zhang, X. Y.; Zheng, Z.; Wu, Y. C. Electrochemical Performance and Biosensor Application of TiO$_2$ Nanotube Arrays with Mesoporous Structures Constructed by Chemical Etching. *Dalton Trans.* **2015**, *44*, 7662−7672.

(34) Si, P.; Ding, S.; Yuan, J.; Lou, X. W.; Kim, D. H. Hierarchically Structured One-Dimensional TiO$_2$ for Protein Immobilization, Direct Electrochemistry, and Mediator-Free Glucose Sensing. *ACS Nano* **2011**, *5*, 7617−7626.

(35) Bian, Z. F.; Zhu, J.; Cao, F. L.; Huo, Y. N.; Lu, Y. F.; Li, H. X. Solvothermal Synthesis of Well-Defined TiO$_2$ Mesoporous Nanotubes with Enhanced Photocatalytic Activity. *Chem. Commun.* **2010**, *46*, 8451−8453.

(36) Li, G. L.; Liu, J. Y.; Jiang, G. B. Facile Synthesis of Spiny Mesoporous Titania Tubes with Enhanced Photocatalytic Activity. *Chem. Commun.* **2011**, *47*, 7443−7445.

(37) Bavykin, D. V.; Passoni, L.; Walsh, F. C. Hierarchical Tube-in-Tube Structures Prepared by Electrophoretic Deposition of Nano-structured Titanates into a TiO$_2$ Nanotube Array. *Chem. Commun.* **2013**, *49*, 7007−7009.

(38) Bao, Z. Q.; Xie, H. X.; Zhu, Q.; Qian, J. S.; Ruan, P.; Zhou, X. F. Microsphere Assembly of TiO$_2$ with Tube-in-Tube Nanostructures: Anisotropic Etching and Photovoltaic Enhancement. *CrystEngComm* **2013**, *15*, 8972−8978.

(39) Yu, Y. H.; Yin, X.; Kvit, A.; Wang, X. D. Evolution of Hollow TiO$_2$ Nanostructures via the Kirkendall Effect Driven by Cation Exchange with Enhanced Photoelectrochemical Performance. *Nano Lett.* **2014**, *14*, 2528−2535.

(40) Roy, P.; Berger, S.; Schmuki, P. TiO$_2$ Nanotubes: Synthesis and Applications. *Angew. Chem. Int. Ed.* **2011**, *50*, 2904−2939.

(41) Sun, D. P.; Yang, J. Z.; Wang, X. Bacterial Cellulose/TiO$_2$ Hybrid Nanofibers Prepared by the Surface Hydrolysis Method with Molecular Precision. *Nanoscale* **2010**, *2*, 287−292.

(42) Luo, Y.; Xu, J. B.; Huang, J. G. Hierarchical Nanofibrous Anatase-Titania−Cellulose Composite and Its Photocatalytic Property. *CrystEngComm* **2014**, *16*, 464−471.

(43) Wang, P. P.; Geng, Z. B.; Gao, J. X.; Xuan, R. F.; Liu, P.; Wang, Y.; Huang, K. K.; Wan, Y. Z.; Xu, Y. Zn$_x$Cd$_{1−x}$S/Bacterial Cellulose Bionanocomposite Foams with Hierarchical Architecture and Enhanced Visible-light Photocatalytic Hydrogen Production Activity. *J. Mater. Chem. A* **2015**, *3*, 1709−1716.

(44) Wang, P. P.; Zhao, J.; Xuan, R. F.; Wang, Y.; Zou, C.; Zhang, Z. Q.; Wan, Y. Z.; Xu, Y. Flexible and Monolithic Zinc Oxide Bionanocomposite Foams by a Bacterial Cellulose Mediated Approach for Antibacterial Applications. *Dalton Trans.* **2014**, *43*, 6762−6768.

(45) Sai, H. Z.; Xing, L.; Xiang, J. H.; Cui, L. J.; Jiao, J. B.; Zhao, C. L.; Li, Z. Y.; Li, F. Flexible Aerogels Based on an Interpenetrating Network of Bacterial Cellulose and Silica by a Non-Supercritical Drying Process. *J. Mater. Chem. A* **2013**, *1*, 7963−7970.

(46) Song, J. L.; Fu, G.; Cheng, Q. S.; Jin, Y. C. Bimodal Mesoporous Silica Nanotubes Fabricated by Dual Templates of CTAB and Bare Nanocrystalline Cellulose. *Ind. Eng. Chem. Res.* **2014**, *53*, 708−714.

(47) Ding, K. L.; Hu, B. J.; Xie, Y.; An, G. M.; Tao, R. T.; Zhang, H. Y.; Liu, Z. M. A Simple Route to Coat Mesoporous SiO$_2$ Layer on Carbon Nanotubes. *J. Mater. Chem.* **2009**, *19*, 3725−3731.

(48) Zhang, Y.; Liu, X.; Huang, J. G. Hierarchical Mesoporous Silica Nanotubes Derived from Natural Cellulose Substance. *ACS Appl. Mater. Interfaces* **2011**, *3*, 3272−3275.

(49) Wang, Y.; Huang, H. B.; Gao, J. X.; Lu, G. Y.; Zhao, Y.; Xu, Y.; Jiang, L. TiO$_2$-SiO$_2$ Composite Fibers with Tunable Interconnected Porous Hierarchy Fabricated by Single-Spinneret Electrospinning toward Enhanced Photocatalytic Activity. *J. Mater. Chem. A* **2014**, *2*, 12442−12448.

(50) Kibombo, H. S.; Peng, R.; Rasalingam, S.; Koodali, R. T. Versatility of Heterogeneous Photocatalysis: Synthetic Methodologies Epitomizing the Role of Silica Support in TiO$_2$ Based Mixed Oxides. *Catal. Sci. Technol.* **2012**, *2*, 1737−1766.

(51) Chen, Q.; Zhou, W.; Du, G. H.; Peng, L. M. Trititanate Nanotubes Made via a Single Alkali Treatment. *Adv. Mater.* **2002**, *14*, 1208−1211.

(52) Yuan, Z. Y.; Zhou, W.; Su, B. L. Hierarchical Interlinked Structure of Titanium Oxide Nanofibers. *Chem. Commun.* **2002**, 1202−1203.

(53) Li, W.; Deng, Y. H.; Wu, Z. X.; Qian, X. F.; Yang, J. P.; Wang, Y.; Gu, D.; Zhang, F.; Tu, B.; Zhao, D. Y. Hydrothermal Etching Assisted Crystallization: A Facile Route to Functional Yolk-Shell Titanate Microspheres with Ultrathin Nanosheets-Assembled Double Shells. *J. Am. Chem. Soc.* **2011**, *133*, 15830−15833.

(54) Bavykin, D. V.; Friedrich, J. M.; Walsh, F. C. Protonated Titanates and TiO$_2$ Nanostructured Materials: Synthesis, Properties, and Applications. *Adv. Mater.* **2006**, *18*, 2807−2824.

(55) Liu, N.; Chen, X.; Zhang, J.; Schwank, J. W. A Review on TiO$_2$-Based Nanotubes Synthesized via Hydrothermal Method: Formation Mechanism, Structure Modification, and Photocatalytic Applications. *Catal. Today* **2014**, *225*, 34−51.

(56) Zhang, H.; Zong, R. L.; Zhao, J. C.; Zhu, Y. F. Dramatic Visible Photocatalytic Degradation Performances Due to Synergetic Effect of TiO$_2$ with PANI. *Environ. Sci. Technol.* **2008**, *42*, 3803−3807.

(57) Pirug, G.; Ritke, C.; Bonzel, H. P. Adsorption of H$_2$O on Ru (001): I. Bilayer and Clusters. *Surf. Sci.* **1991**, *241*, 289−301.

(58) Yan, J. Q.; Wu, G. J.; Guan, N. J.; Li, L. D.; Li, Z. X.; Cao, X. Z. Understanding the Effect of Surface/Bulk Defects on the Photo-catalytic Activity of TiO$_2$: Anatase versus Rutile. *Phys. Chem. Chem. Phys.* **2013**, *15*, 10978−10988.

(59) Ulusoy, T. G.; Ghobadi, A.; Okyay, A. K. Surface Engineered Angstrom Thick ZnO-sheathed TiO$_2$ Nanowires as Photoanodes for Performance Enhanced Dye-Sensitized Solar Cells. *J. Mater. Chem. A* **2014**, *2*, 16867−16876.

(60) Jing, L. Q.; Qu, Y. C.; Wang, B. Q.; Li, S. D.; Jiang, B. J.; Yang, L. B.; Fu, W.; Fu, H. G.; Sun, J. Z. Review of Photoluminescence Performance of Nano-Sized Semiconductor Materials and Its Relationships with Photocatalytic Activity. *Sol. Energy Mater. Sol. Cells* **2006**, *90*, 1773−1787.

(61) Kernazhitsky, L.; Shymanovska, V.; Gavrilko, T.; Naumov, V.; Fedorenko, L.; Kshnyakin, V.; Baran, J. Laser-Excited Excitonic Luminescence of Nanocrystalline TiO$_2$ Powder. *Ukr. J. Phys.* **2014**, *59*, 246−253.